Electronic Supplementary Material (ESI) for Chemical Science.

Supplementary Information

From wavelike to sub-diffusive motion: Exciton dynamics and interaction in squaraine copolymers of varying length

Pavel Malý[a], Julian Lüttig[a], Arthur Turkin[b], Jakub Dostál[a], Christoph Lambert*[b,c], and Tobias Brixner*[a,c]

[a]*Institut für Physikalische und Theoretische Chemie, Universität Würzburg, Am Hubland, 97074 Würzburg, Germany*
[b]*Institut für Organische Chemie, Universität Würzburg, Am Hubland, 97074 Würzburg, Germany*
[c]*Center for Nanosystems Chemistry (CNC), Universität Würzburg, Theodor-Boveri-Weg, 97074 Würzburg, Germany*
**christoph.lambert@uni-wuerzburg.de*, **brixner@phys-chemie.uni-wuerzburg.de*

Contents

S1 Theory

Excitonic States

We construct a Frenkel exciton model of exciton–exciton interaction (EEI) in molecular aggregates and conjugated polymers. Each molecule is modelled as a three-level electronic system interacting with its environmental bath with a Hamiltonian

$$H_n = |g_n\rangle e_g \langle g_n| + |e_n\rangle \Big(e_n + \delta e_n + \Delta V_n\big(Q(t)\big)\Big) \langle e_n| + |f_n\rangle \Big(e_n + \delta e_n + e_f + \Delta V_n^f\big(Q(t)\big)\Big) \langle f_n|.$$

Here $|g_n\rangle$ is the ground state, $|e_n\rangle$ the first excited state, and $|f_n\rangle$ the higher excited state. The state energies are e_g, e_n, and $e_n + e_f$, respectively. We set $e_g = 0$ and consider the transition energies with respect to the ground state. δe_n is the energetic disorder (for which later we assume Gaussian disorder and average over it), $\Delta V_n(Q(t))$ is the energy-gap operator in the first excited state, and $\Delta V_n^f(Q(t))$ the same operator for the higher excited state. These reflect the molecular energy-gap fluctuations due to the bath coordinates *Q*. The index *n* = 1, …, *N* labels the chromophores. We describe the bath by the spectral density of the modes, $C(\omega)$, which is a Fourier transform of the energy-gap correlation function:

$$C(\omega) = \int dt\, \mathrm{e}^{i\omega t} \langle \Delta V(t) \Delta V(0) \rangle.$$

This can be written as

$$C(\omega) = \left(1 + \operatorname{cotanh} \frac{\hbar\omega}{2k_B T}\right) C''(\omega)$$

with

$$C''(\omega) = \frac{2\lambda\Lambda}{\omega^2 + \Lambda^2} + \frac{2\lambda_v \Omega^2 \omega\gamma}{(\Omega^2 - \omega^2)^2 + \omega^2\gamma^2}.$$

Here we have introduced in the first term an overdamped Brownian oscillator model for the bath, with reorganization energy λ (Stokes' shift is 2λ) and inverse correlation time (i.e., memory) Λ. The second term is an underdamped oscillator with frequency Ω, reorganization energy $\lambda_v = S\Omega$ (S is the Huang-Rhys factor), and (weak) damping γ. We consider the same spectral density for each of the chromophores, both in the first and higher excited state.

The total Hamiltonian of the molecular aggregate or polymer consists of *N* chromophores and the coupling between their transitions. We formulate the problem in the collective states,

$$|g\rangle = |g_1\rangle \dots |g_N\rangle,$$

$$|e\colon n\rangle = \ |g_1\rangle \ldots |e_n\rangle \ldots |g_N\rangle,$$

$$|e\colon nm\rangle = |g_1\rangle \ldots |e_n\rangle \ldots |e_m\rangle \ldots |g_N\rangle,$$

$$|e\colon nml\rangle = |g_1\rangle \ldots |e_n\rangle \ldots |e_m\rangle \ldots |e_l\rangle \ldots |g_N\rangle,$$

where $|g\rangle$ denotes the overall ground state and $|e\colon n\rangle$, $|e\colon nm\rangle$, and $|e\colon nml\rangle$ states in which one, two, or three chromophores, respectively, are in the first excited state. The rows in the formula above define the zero-, one-, two-, and three-quantum state manifolds, respectively. Apart from the first excited states, we also include higher excited two-quantum states of each molecule,

$$|f\colon n\rangle = \ |g_1\rangle \ldots |f_n\rangle \ldots |g_N\rangle,$$

wherein chromophore *n* is in its higher excited state, and the three-quantum states

$$|f\colon n, e\colon m\rangle = \ |g_1\rangle \ldots |f_n\rangle \ldots |e_m\rangle \ldots |g_N\rangle,$$

wherein chromophore *n* is in its higher excited state and chromophore *m* in its first excited state. The states are schematically depicted in Fig. S1, together with the system parameters used further in the text.

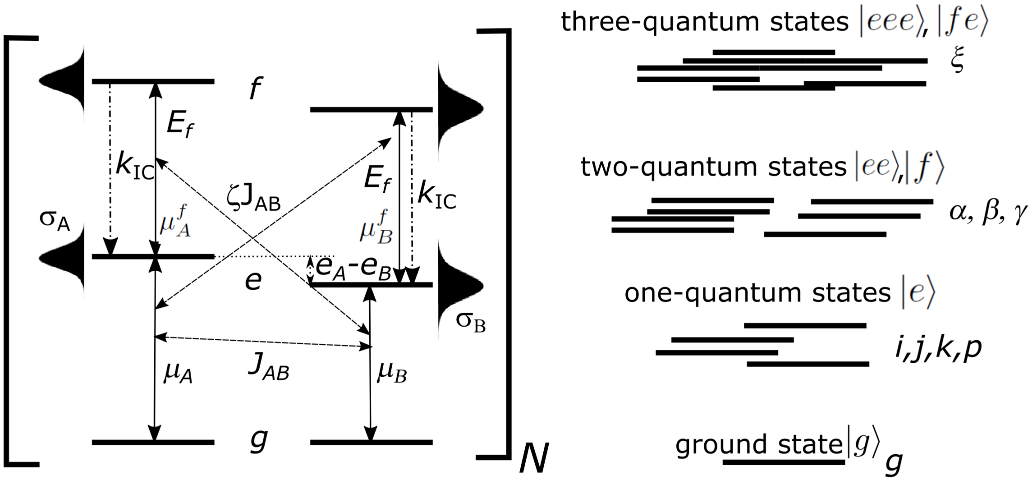

Figure S1. Parameters of the squaraine SQA-SQB dimer units (left) and the state structure arising from diagonalization of the corresponding Hamiltonian (right). As the polymer is composed of identical units, the distinction into dimers is somewhat arbitrary.

The total aggregate or copolymer Hamiltonian then reads

$$H_{\text{agg}} = |g\rangle e_g \langle g| + \sum_{n} |e{:}\,n\rangle (e_n + \delta e_n) \langle e{:}\,n| + \sum_{n<m} |e{:}\,nm\rangle (e_n + \delta e_n + e_m + \delta e_m) \langle e{:}\,nm|$$

$$+ \sum_{n} |f{:}\,n\rangle (e_n + e_f + \delta e_n) \langle f{:}\,n| + \sum_{n,m} |f{:}\,n, e{:}\,m\rangle (e_n + e_f + \delta e_n + e_m + \delta e_m) \langle f{:}\,n, e{:}\,m|$$

$$+ \sum_{n<m} |e{:}\,nml\rangle (e_n + \delta e_n + e_m + \delta e_m + e_l + \delta e_l) \langle e{:}\,nml|$$

$$+ \sum_{n\neq m} |e{:}\,n\rangle J_{nm} \langle e{:}\,m| + \sum_{n<m,k<l} |e{:}\,nm\rangle J_{e:nm;e:kl} \langle e{:}\,kl| + \sum_{n<m<p,k<l<q} |e{:}\,nmp\rangle J_{e:nmp;e:klq} \langle e{:}\,klq|$$

$$+ \sum_{n<m,k} \big(|e{:}\,nm\rangle J_{e:nm;f:k} \langle f{:}\,k| + |f{:}\,k\rangle J_{e:nm;f:k} \langle e{:}\,nm| \big) + \sum_{n\neq k, m\neq l} |f{:}\,n, e{:}\,k\rangle J_{f:n,e:k;f:m,e:l} \langle f{:}\,m, e{:}\,l|.$$

The first three lines comprise the diagonal elements, the energies of the zero-quantum ($|g\rangle$), one-quantum ($|e{:}\,n\rangle$), and two-quantum states. The last two lines describe the couplings between the transitions between the states differing by one quantum (of visible light needed for the optical transition). The coupling between the one-exciton transitions in chromophores *n* and *m* is J_{nm}. The couplings between two-exciton states follows to be $J_{\text{e:nm;e:kl}} = J_{\text{nk}}\delta_{ml} + \delta_{nk}J_{ml}$ (δ_{ij} is the Kronecker delta) and analogously pairwise for the three-exciton states. The coupling for the transitions to the higher states is $J_{\text{e:nm;f:k}}$, and the coupling between the three-quantum states is $J_{\text{f:n,e:k;f:m,e:l}}$. For simplicity we consider $J_{\text{e:nm;f:k}} = \zeta(\delta_{kn} + \delta_{km})J_{\text{nm}}$, where ζ is simply a proportionality factor. In our particular case we consider only the coupling between the transitions on neighbouring chromophores along the polymer chain, see also section 'Inter-chain transfer discussion' below.

The total transition dipole-moment operator reads

$$\mu = \sum_{n} (|g\rangle \mu_n \langle e{:}\,n| + h.c.) + \sum_{n<m} (|e{:}\,nm\rangle \mu_n \langle e{:}\,m| + |e{:}\,nm\rangle \mu_m \langle e{:}\,n| + h.c.)$$

$$+ \sum_{n} \big(|f{:}\,n\rangle \mu_n^f \langle e{:}\,n| + h.c. \big) + \sum_{n\neq m, k<l} \big(|f{:}\,n, e{:}\,m\rangle \mu_n^f (\delta_{nk}\delta_{ml} + \delta_{nl}\delta_{mk}) \langle e{:}\,kl| + h.c. \big)$$

$$+ \sum_{n<m<l, p<q} |e{:}\,nml\rangle \big(\delta_{mp}\delta_{lq}\mu_n + \delta_{np}\delta_{lq}\mu_m + \delta_{np}\delta_{mq}\mu_l \big) \langle e{:}\,pq|.$$

Here μ_n is the transition dipole moment from the ground to the first excited state of the *n*-th chromophore, and μ_n^f is the transition dipole moment from the first excited state to a higher excited state. In the same spirit as with the couplings, we consider for simplicity $\mu_n^f \propto \mu_n$ (with a different proportionality constant compared to the case for the couplings, see Table S1 below).

For further consideration, the total Hamiltonian is diagonalized,

$$H_e = C^T H_{\text{agg}} C,$$

where C is the orthonormal transformation matrix with coefficients c_n^i (*n* for chromophores and *i* for excitons) and C^T its transposed matrix. This transformation yields the (multi)excitonic states, with energies ϵ_i on the diagonal of H_e, as indicated also in Fig. S1 right.

Also the transition dipole-moment operator is transformed into the excitonic basis:

$$\mu_e = C^T \mu C.$$

System Dynamics

The dynamics of the excitons consist of exciton transfer and EEI (i.e., annihilation). The exciton transfer is calculated by Redfield theory,[1] i.e., second-order perturbation theory in the interaction with the bath, described by a spectral density $C(\omega)$, leading to transition rates k_{ij} from exciton $|j\rangle$ to exciton $|i\rangle$,

$$k_{ij} = \sum_n \left|c_n^i\right|^2 \left|c_n^j\right|^2 \nu_n C(\omega_{ji}).$$

Here c_n^i are the elements of the transformation matrix *C*, reflecting the co-localization of excitons *i*, *j* on chromophore *n*, $\hbar\omega_{ji} = \epsilon_j - \epsilon_i$ is the excitonic energy gap, and ν_n is the scaling of the strength of the interaction of molecule *n* with the bath.

The transfer between two-exciton states (from state β to α) is also calculated by Redfield theory,[2]

$$k_{\alpha\beta}^{ee} = \sum_{n<m,k<l} (\delta_{nk} + \delta_{nl} + \delta_{mk} + \delta_{ml}) c_{nm}^{\alpha} c_{nm}^{\beta} c_{kl}^{\alpha} c_{kl}^{\beta}\, C\big(\omega_{\beta\alpha}\big),$$

where c_{nm}^{α} are the respective elements of the transformation matrix to the multi-exciton basis.

If we take the energy-gap function of the higher excited $|f_n\rangle$ states proportional to that of the $|e_n\rangle$ states, with proportionality constant ϕ, energy-gap fluctuations between the $|f_n\rangle$ and $|e_n\rangle$ states partially correlated (reflected by $\phi_{\text{corr}} \in [0,1]$), then the $|f_n\rangle$ states contribute to the two-exciton transfer by the following two terms:

$$k_{\alpha\beta}^{fee} = \phi_{\text{corr}} \phi \sum_{n<m,k} (\delta_{nk} + \delta_{mk}) c_{nm}^{\alpha} c_{nm}^{\beta} c_{f_k}^{\alpha} c_{f_k}^{\beta}\, C\big(\omega_{\beta\alpha}\big),$$

$$k_{\alpha\beta}^{f} = \phi^2 \sum_n \left|c_{f_n}^{\alpha}\right|^2 \left|c_{f_n}^{\beta}\right|^2 C(\omega_{\alpha\beta}).$$

The first term arises from the possible correlation of the $|f_n\rangle$ and $|e_n\rangle$ state environmental fluctuations. In our calculation we set a weak correlation of $\phi_{\mathrm{corr}} = 0.1$, but the correlation influence is weak in our parameter range anyway. The second term is the contribution purely from the $|f_n\rangle$ states. The overall transfer rate in the two-quantum manifold is

$$k_{\alpha\beta} = k_{\alpha\beta}^{ee} + k_{\alpha\beta}^{fee} + k_{\alpha\beta}^{f}.$$

We use a secular approximation, separating the evolution of the population from coherences. Furthermore, we will not treat the coherence dynamics, as this reduces significantly the computational effort. Any oscillatory dynamics of the signal due to the excitonic coherent motion will thus be neglected.

In the process of exciton–exciton annihilation, the two-exciton state changes into a higher chromophore-excited state $|f_n\rangle$, which then rapidly relaxes with an internal conversion rate k_{IC}. As can be derived using a Lindblad formalism,[3] the decay of the mixed two-quantum state $|\alpha\rangle$ into a (one-quantum) exciton $|k\rangle$ is

$$k_{k\alpha} = \sum_n \left|c_n^k\right|^2 \left|c_{f_n}^{\alpha}\right|^2 k_{\mathrm{IC}}.$$

Finally, to get the correct long-time dynamics of the system, one has to consider the finite lifetime τ_R of the excitons due to radiative and non-radiative recombination. Due to the separation of timescales, the details of this process are not relevant and it is sufficient to take into account the exciton relaxation to the ground state with a rate constant $k_{\mathrm{R}} = \tau_{\mathrm{R}}^{-1}$.

The evolution of the system as a function of waiting time is, in this rate picture, given by the equation

$$\frac{d\rho(t)}{dt} = \mathcal{K}\rho(t),$$

where $\rho(t)$ is the system density matrix at time t and $\mathcal{K}$ is the matrix with all the rates, with the elements given by the rate expression given above. This equation is solved with help of a time-evolution propagator $\mathcal{U}(T)$,

$$\rho(T) = \mathcal{U}(T)\rho(0),$$

starting from the equilibrium density matrix $\rho(0)$, with

$$\mathcal{U}(T) = \exp(\mathcal{K}T).$$

The elements of the propagator matrix $\mathcal{U}(T)$, denoted for instance $\mathcal{U}_{ii,jj}(T)$, contain conditional probabilities for the system starting at time zero in a particular state (here $|j\rangle$) to be after time T in another particular state (here $|i\rangle$).

Optical Response

The system response to the action of the pulses is formulated in a response-function formalism. The EEI2D signal is a fifth-order response to the interaction with the three pulses, twice with each of the two pump pulses and once with the probe pulse. The response is formulated by following the evolution of the system in Liouville space (i.e., following its density matrix), and keeping track of the interactions with the laser pulses. The interaction with light is described in a dipole approximation:

$$H_{\mathrm{int}}(t) = -\mu E(t).$$

In an impulsive limit (physical δ pulses), the total polarization of fifth order is then

$$P^{(5)}(t,T,\tau) \propto \left(\frac{i}{\hbar}\right)^{5} \mathrm{Tr}_{\mathrm{B}} \left\{ \mu\,\mathcal{U}(t) \left[\mu, \mathcal{U}(T) \left[\mu, \left[\mu, \mathcal{U}(\tau) \left[\mu, \left[\mu, \rho_{\mathrm{eq}} \otimes W_{\mathrm{eq}}\right]\right]\right]\right]\right] \right\} E_{\mathrm{pr}} I_{\mathrm{pu}}^{2}.$$

Here E_{pr} is the probe electric field and I_{pu} the intensity of the pump field, ρ the system density matrix, W the density matrix of the vibrational bath, and Tr_{B} signifies tracing over bath coordinates. The subscripts "eq" denote that the system and the bath are in the ground-state equilibrium before the action of the pulses. The fifth-order signal field is proportional to the fifth-order polarization, assuming perfect phase matching:

$$E_{\mathrm{sig}}^{(5)}(t,T,\tau) \propto\; i\omega\, P^{(5)}(t,T,\tau).$$

Such a response includes many terms, which are conveniently followed using Liouville-space pathways. When one integrates over the spectral response both on the excitation and detection axis, each pathway contributes only with a factor composed of six transition-dipole elements. The time evolution in the waiting time T is given by the rates calculated in the previous section.

In Fig. S2 all the rephasing Liouville-space pathways contributing to the signal are depicted. These pathways are summed over all the contributing states, with the appropriate sign given by the number of the interactions from the right (due to the commutators in the equation above).

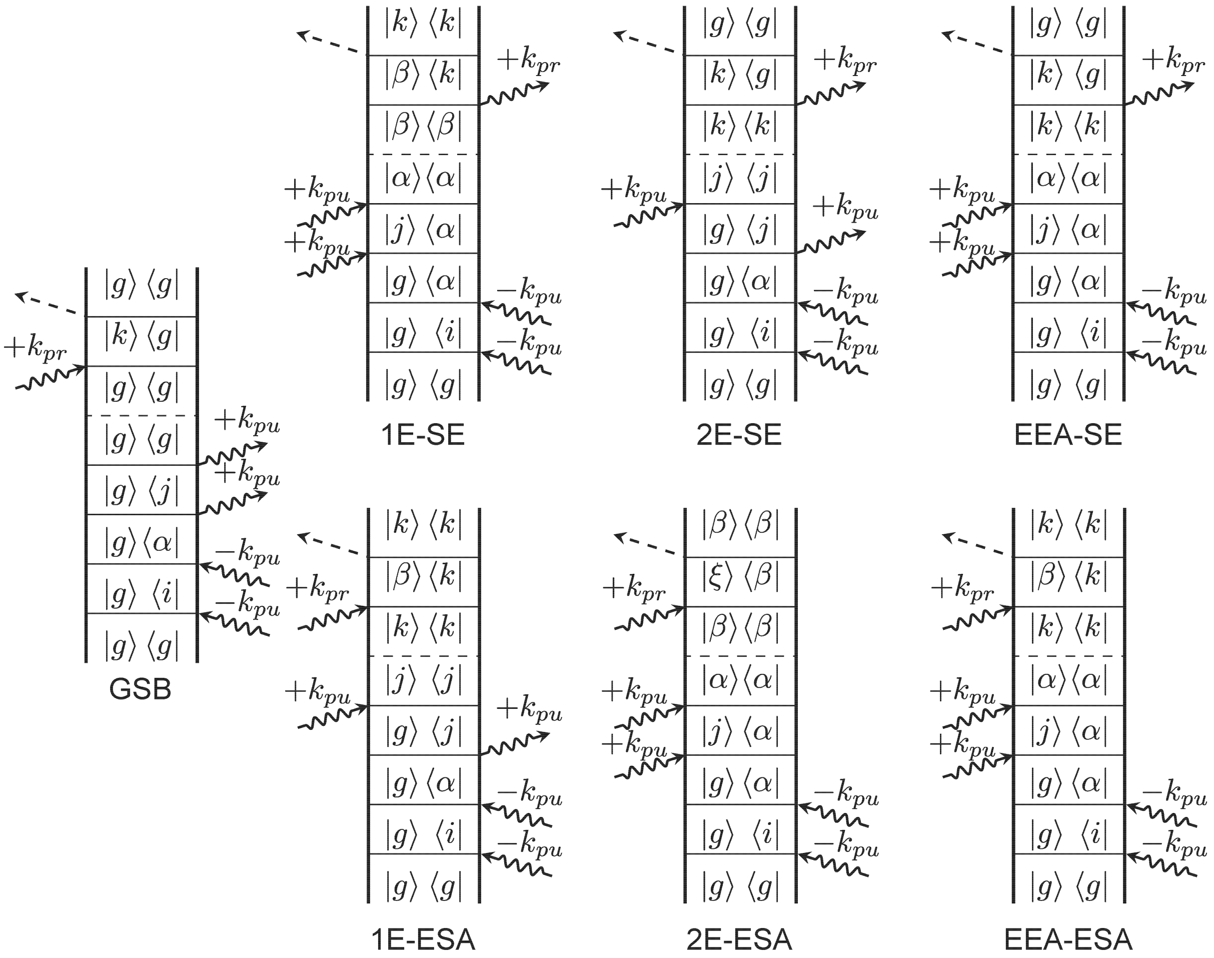

Figure S2. Double-sided Feynman diagrams for calculation of the optical response. Solid curvy arrows indicate interaction with the electric field, dashed arrows indicate generation of the coherent polarization response, dashed horizontal lines indicate propagation during waiting time *T*. Index *g* denotes the ground state, *i,j,k* denote one-exciton (i.e., one-quantum) states, α, β denote two-quantum states (i.e., two-exciton states mixed with higher excited states), and ξ denotes a three-quantum state. The states are depicted in Fig. S1.

To give an example, from these diagrams one can immediately deduce that the spectrally integrated two-exciton stimulated-emission pathway contribution can be calculated as

$$\text{2E-SE}(T) = \sum_{i,\alpha,j,\beta.k} \mu_{ig}\mu_{\alpha i}\mu_{jg}\mu_{\alpha j}\mu_{\beta k}\mu_{\beta k}\mathcal{U}_{\beta\beta,\alpha\alpha}(T),$$

and analogously for all the other pathways.

In the numerical calculations first the matrix of the transition dipole moment and the rate matrix are pre-calculated. Then, for each population time step, the propagator matrix is calculated taking the matrix exponential. Finally, the pathway amplitudes are summed together, yielding a single number for each population time: the fifth-order signal amplitude.

High-Power Correction

In the experiment, a power dependence of the signal dynamics is observed. This can be explained by an increased excitation density at very high excitation powers, leading to a more probable exciton–exciton annihilation. Exciton–exciton annihilation is a two-exciton process, and in the fifth-order EEI2D spectroscopy we are probing the dynamics of two-exciton states. When the direct contribution of the higher molecular excited state is negligible (compared to the two-exciton contribution), the signal is proportional to the annihilated two-exciton states. Therefore, the probability of populating a particular two-exciton state is evaluated when calculating the system response. And for every two-exciton state, annihilation kinetics result as a property of the system only, regardless of the excitation power. As a result, in fifth-order EEI2D spectra, the signal amplitude only should increase with excitation power, but the kinetics (i.e., the time evolution), should remain unchanged. Any observed change in the kinetics therefore has to be an effect of higher order, that is, of the influence of other excitons present in the system, but not probed directly by our fifth-order signal. In order to account for the high-power effects, we therefore have to include a higher-order correction. We do this in the following way: For each Liouville-space pathway, we add the possibility of the probed one-exciton or two-exciton state to meet another exciton, which can lead to an annihilation event. For the one-exciton population of state $|j\rangle$, the probability of this event is given by the chance of this exciton $|j\rangle$ being part of a two-quantum state $|\gamma\rangle$, multiplied by the probability that this state is excited, P(γ), and multiplied by the probability that this two-quantum state relaxes to a one-quantum state different than the original one,

$$\mathcal{U}_{gg,jj}(T) = \sum_{p \neq j,\gamma} P(\gamma)\pi(j,\gamma)\mathcal{U}_{pp,\gamma\gamma}(T),$$

where we denoted the probability of exciton $|j\rangle$ to be in the two-quantum state $|\gamma\rangle$ as

$$\pi(j,\gamma) = \sum_{n<m} \left|c_n^j\right|^2 \left|c_{nm}^\gamma\right|^2.$$

For the two-exciton state we should in principle also take into account the three-exciton state dynamics. This is, however, not computationally feasible. We therefore assume factorization in the sense of the excitonic densities so that the two-exciton probability is a product of one-exciton probabilities. The annihilation of a two-exciton state $|\gamma\rangle$ is then augmented by the chance that one of the excitons part of $|\gamma\rangle$ meets another exciton from a different two-exciton state and they annihilate. This modifies the time-evolution propagator matrix elements as follows:

$$\mathcal{U}_{kk,\alpha\alpha}(T) \rightarrow \mathcal{U}_{kk,\alpha\alpha}(T) + \sum_{p,\gamma \neq \alpha} P(\gamma)\pi(p,\alpha)\pi(p,\gamma)\mathcal{U}_{kk,\gamma\gamma}(T).$$

The population of the high-intensity-induced two-exciton states, *P(γ)*, is proportional to the transition strength of all possible ways to reach this two-exciton state and the (normalized) intensity of the excitation $I = \left|E_{\mathrm{pu}}\right|^2$:

$$P(\gamma) = \sum_i |\mu_{ig}|^2 |\mu_{\gamma i}|^2 \, |E_{\mathrm{pu}}|^2.$$

Put together, one obtains corrected propagators connecting the two-quantum with one-quantum, and one-quantum with zero-quantum manifold, where the magnitude of the correction depends on the excitation intensity. When evaluating the response pathways, this additional annihilative channels are then present.

Calculation parameters: choice and robustness

In Table S1 the parameters used for the calculations are given. The parameters connected to the one-quantum transitions, and therefore the absorption and emission spectra (transition energies, coupling, energy gap, transition dipole moments, reorganization energy, vibrational mode parameters), were taken from SQA-SQB dimer studies[4] and slightly re-adjusted to better fit our experimental data. The exception is the electronic coupling, whose absolute magnitude had to be decreased from the estimated 710–780 cm^{-1} of the previous workon SQA-SQB dimers[4] to -420 cm^{-1}, in agreement with the previous work on squaraine copolymers[5,6] where the coupling of -480 cm^{-1} is used. We note here that, assuming the same energy gap between the SQA and SQB transitions as for the monomers, the coupling magnitude is fairly fixed by the excitonic splitting, see Fig. S5a for illustration. This splitting is larger in the polymers, because of the increasing delocalization length with the chain length. Such an effect of increased delocalization is well-known from J-aggregates, with which the conjugated polymers share many properties.[7] The increasing delocalization was investigated in detail by Spano in the spectroscopic context.[8] The reduced coupling value of -420 cm^{-1}, assumed for the polymer in the present work, as compared to $\sim$750 cm^{-1} for a dimer, thus most probably reflects the polymer structural disorder, which decreases the delocalization length.[9] The value used in this and the cited works can thus be regarded as effective coupling.

The parameters of the higher excited states (energy difference from the lowest excited states, coupling to the bath, *f*-*e* transition dipole moments) were set similar to the one-quantum transitions, and scaled to fit the system dynamics. The energies of the higher-lying $|f\rangle$ states were derived from the linear absorption spectrum in the corresponding wavelength region, see Fig. S3. We note that while there is actually a number of higher states, we describe them as one effective state, which couples to the two-exciton state. As the only important property of the higher-lying states is their mixing with the two-exciton states, on our level of description, the effect of changing the coupling between the *e*-*g* and *f*-*e* transitions is the same as changing the density of states. The internal conversion time was varied only between 20 and 50 fs, based on independent nonlinear measurements of exciton–exciton annihilation in SQA-SQB dimers (see Fig. S4). There we have measured standard, fluorescence-detected 2DES spectra of SQA-SQB dimers in toluene, at high excitation power. Taking the amplitude of the lower-energy diagonal peak (which does not exhibit energy transfer dynamics), we observe a decay in population time, together with some coherent oscillations on top. While the oscillations can be ascribed to the vibrational mode ($1280\ \mathrm{cm}^{-1}$ which corresponds to a period of 26 fs), the decay is caused by the exciton–exciton annihilation.

Table S1. Parameters for the theoretical simulations (for ease of comparison all quantities were converted to wavenumbers or femtoseconds).

Quantity	Variable	Value
SQB transition energy	e_B	13500 cm^{-1}
SQA-SQB energy gap	$e_A - e_B$	1200 cm^{-1}
Transition energy between first and higher excited state	E_f	12200 cm^{-1}
Electronic coupling between one-exciton transitions	J_{AB}	-420 cm^{-1}
Higher-state transition coupling scaling	J_{fe}/J_{eg}	2
Energetic disorder width	$\sigma_A^{\mathrm{FWHM}},\ \sigma_B^{\mathrm{FWHM}}$	250 cm^{-1}, 500 cm^{-1}
One-exciton transition dipole moments	$\mu_A,\ \mu_B$	1.2, 1.0
Transition dipole to higher states scaling	$\mu_{A,B}^f\ /\mu_{A,B}$	0.33
Scaling of coupling to the bath	ν_A, ν_B	1.0, 1.66
Scaling of coupling to the bath for higher excited states	$\nu_{A,B}^f/\nu_{A,B}$	4.0
Bath reorganization energy	λ	180 cm^{-1}
Bath inverse correlation time	Λ	300 cm^{-1}
Strong vibrational mode parameters: frequency, damping, H-R factor	Ω, γ, S	1280 cm^{-1}, 10 cm^{-1}, 0.18
Exciton lifetime dependence on polymer length *N*	τ_R	$(1710.2 - 61.9N)$ ps
Internal conversion time	τ_{IC}	30 fs
Exciton annihilation time in a dimer	$\tau_{\mathrm{ann}}^{\mathrm{dim}}$	30 fs

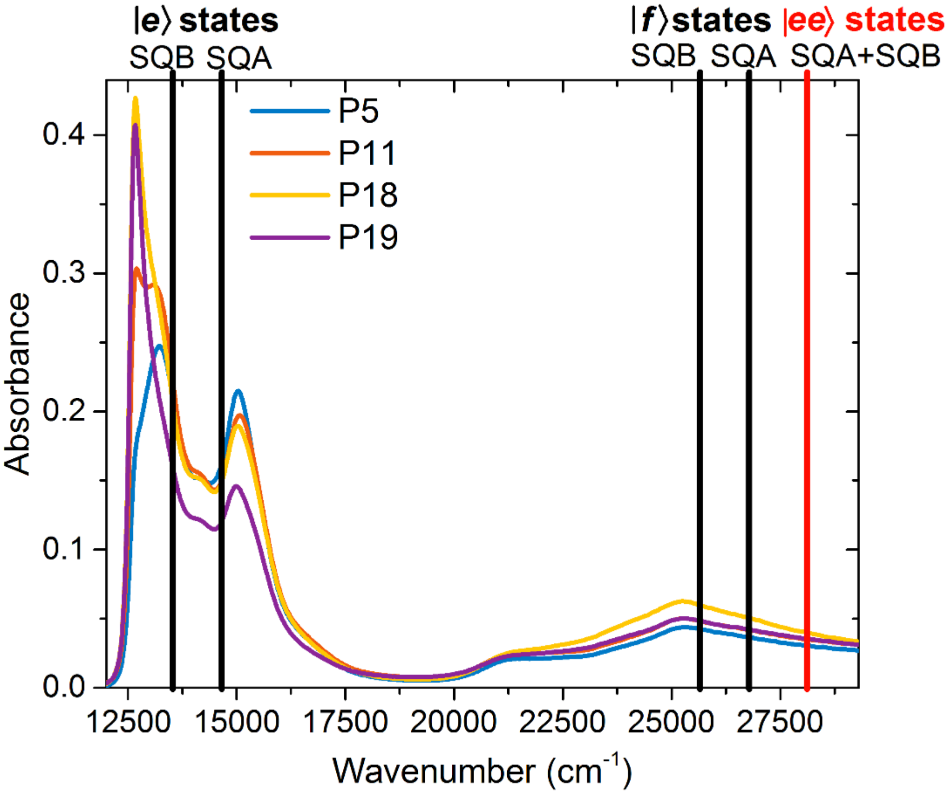

Figure S3. Position of diabatic states used for the theoretical model, compared to the polymer absorption spectrum. Depicted are the diabatic (i.e., site basis, before excitonic splitting) one-exciton SQA and SQB $|e\rangle$ states, the higher SQA and SQB $|f\rangle$ states, and the two-exciton $|ee\rangle$ states. As a result of the coupling between the electronic transitions, the states mix and exhibit excitonic splitting.

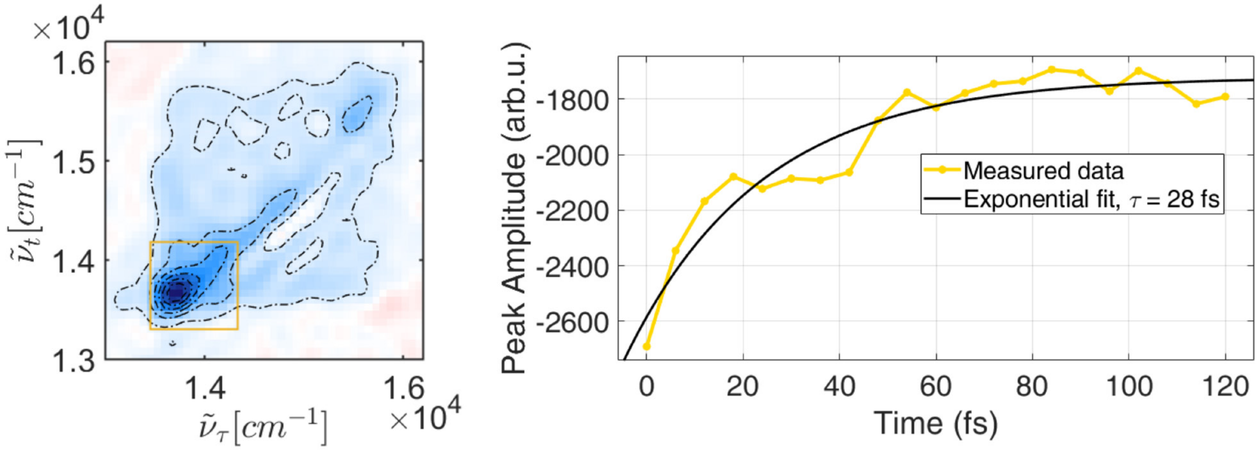

Figure S4. Fluorescence-detected 2DES of SQA-SQB dimers at high excitation intensity (120 nJ at pulse overlap), used here to obtain the annihilation time in SQA-SQB dimers. Left: Absorptive spectrum at $T = 0$ fs, with indicated region of interest (yellow square) around the lower-energy peak, the amplitude of which decays over population time due to annihilation. Right: Decay of the lower-energy peak amplitude (yellow), fitted with an exponential (black) with time constant 28 fs, verifying the 30 fs annihilation time in a SQA-SQB dimer used to describe the polymer dynamics.

Even though we used as many independent constraints on the parameters as possible, our model is based on various approximations. As such, it is important to verify that our results are robust against reasonable parameter variation. To this end, we have investigated the model behavior under parameter variation. The key feature is the exciton delocalization, arising due to the coupling between the chromophoric transitions. We have thus varied the coupling from -200 cm^{-1} to -800 cm^{-1}, some of the effects are illustrated in Fig. S5. With increasing coupling, the split of the absorption peaks becomes larger, the initial exciton delocalization increases, the diffusion coefficient at 1 ps increases [from *D*(1 ps) = 11.5 SQAB^2 for J = -200 cm^{-1} to *D*(1 ps) = 210 SQAB^2 for J = -800 cm^{-1}], and the anomalous diffusion coefficient varies from 0.56 to 0.15. While quantitatively these are large changes, qualitatively the exciton dynamics retains its character of anomalous diffusion. Similar conclusions apply to other parameters such as the energy gaps, energetic disorder, and bath parameters, although their effect is not as drastic as that of the coupling. The strong coupling dependence underlines the importance of the exciton delocalization length relative to the size of the polymer for the exciton dynamics and interaction.

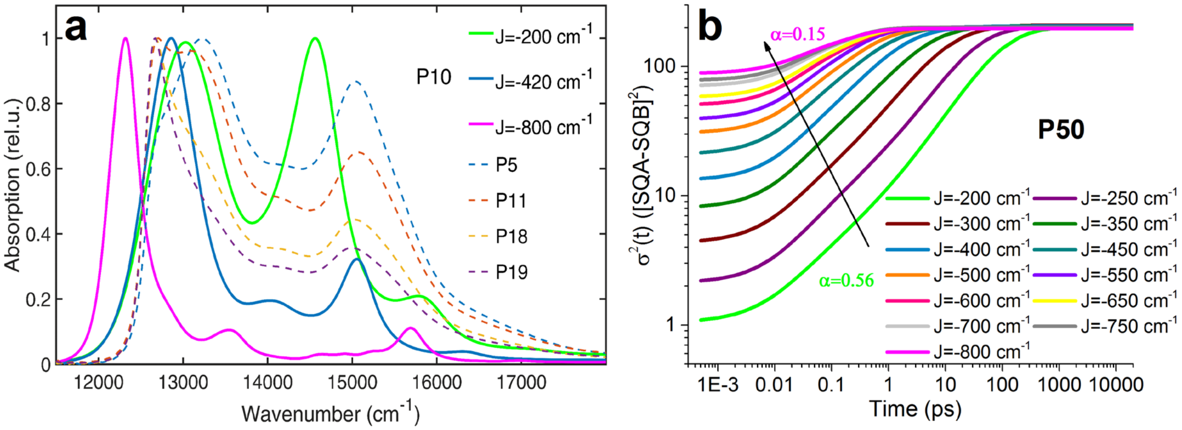

Figure S5. Variation of simulated results with electronic coupling *J*. (a) The sensitivity of the peak splitting in the linear absorption spectrum on the electronic coupling puts a strong constraint on the coupling magnitude. (b) With increasing absolute magnitude of the coupling (indicated by a black arrow), the excitons become more delocalized at early times and, in a polymer of given length (here 50 dimers), the exciton diffusion becomes more anomalous.

Linear Spectra

Here in Fig. S6 we present the measured (dashed) and calculated (solid) linear absorption (Fig. S6a) and fluorescence (Fig. S6b) spectra for the four investigated polymers.

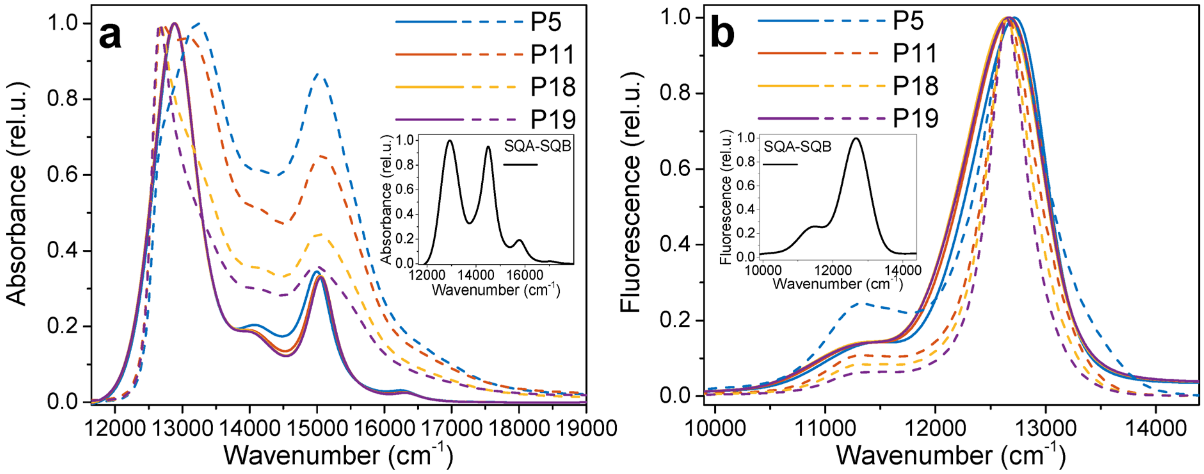

Figure S6. Linear spectra displaying (a) absorption and (b) fluorescence of the P5 (blue), P11 (orange), P18 (yellow), and P19 (violet) polymer for experiment (dashed lines) and theory (solid lines). Insets: Calculated spectra of SQA-SQB dimers. In the experimental spectra a progressive narrowing with increasing polymer length can be observed, which could indicate possible increased exchange narrowing. This trend is, however, not observed in the theoretical spectra. A possible explanation is the relatively local (with respect to the polymer size) character of the excitons. The narrowing can then possibly be caused by a small local stabilization of the polymer conformation.[9]

Direct observation of higher excited states

As we mention in the main text, in principle in the initial ultrafast phase of the signal evolution also the internal conversion of the higher-excited states directly contributes to the observed kinetics. However, in an extended multi-chromophoric system such as the polymer (starting from a size of ten monomers for P5 and increasing for the other samples), the contribution of two-exciton states (which is necessarily present), vastly dominates over the direct higher excited $|f\rangle$ states. The main reason is plainly the number of two-exciton states, which scales as $N(N-1)/2$, compared to N for the higher-excited states. We can quantify the relative contributions of the two signals by (hypothetically) decoupling the two-exciton states from the higher $|f\rangle$ states, thus disabling the annihilation. As is demonstrated in Fig. S7, as a result the fifth-order signal practically disappears (red curve) as compared to the main case with annihilation (blue curve). This clearly shows the dominating role of the bi-exciton kinetics. For detailed investigation of smaller (dimeric, trimeric) systems we refer the reader to Ref. [10].

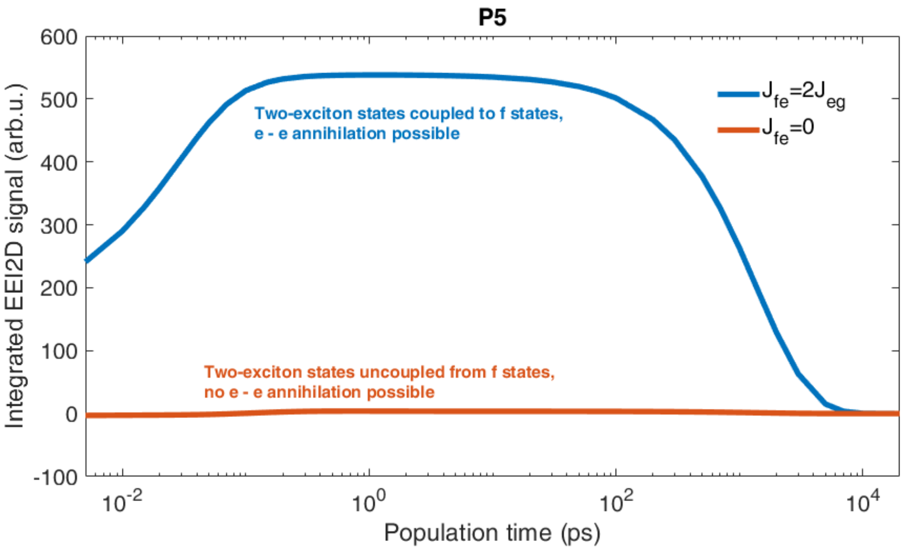

Figure S7. Integrated EEI2D signal with (blue) and without (orange) exciton–exciton annihilation.

Data fitting

In Fig. S8 the fitted linear decrease of the exciton lifetime with the polymer length is shown. The dependence was used for the decay of the calculated kinetic traces, which is not sensitive on the precise value of the decay time. For details and data on the lifetime measurement by TCSPC see Section S2 below.

In Fig. S9 we show how we determine the threshold for the colored rectangular regions in Fig. 3a of the main text that indicate when the signal reaches its plateau. The integrated EEI2D signals as a function of population time (Fig. S9, symbols) are fitted by Lorentzian functions in logarithmic time scale to describe the peak regions for each polymer length (Fig. S9, colored solid lines), and from the fitted curves the times when the signal rises and drops to the 90% of its maximum value are extracted and plotted as black rectangles in Fig. S9 and as colored rectangles in Fig. 3a of the main text.

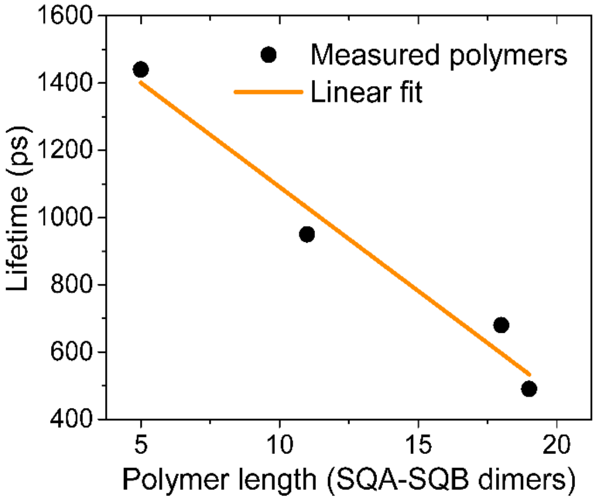

Figure S8. Linear fit (orange) of the experimentally measured (black circles) excitation lifetime that decreases with polymer length. The extracted linear dependence $\tau_R = 1710.2 - 61.9N$, where N indicates the number of SQA–SQB dimers (see also Table S1 above), was used for the excitation lifetime in the kinetic trace calculations in Figs. 3, 4 and 5 of the main text.

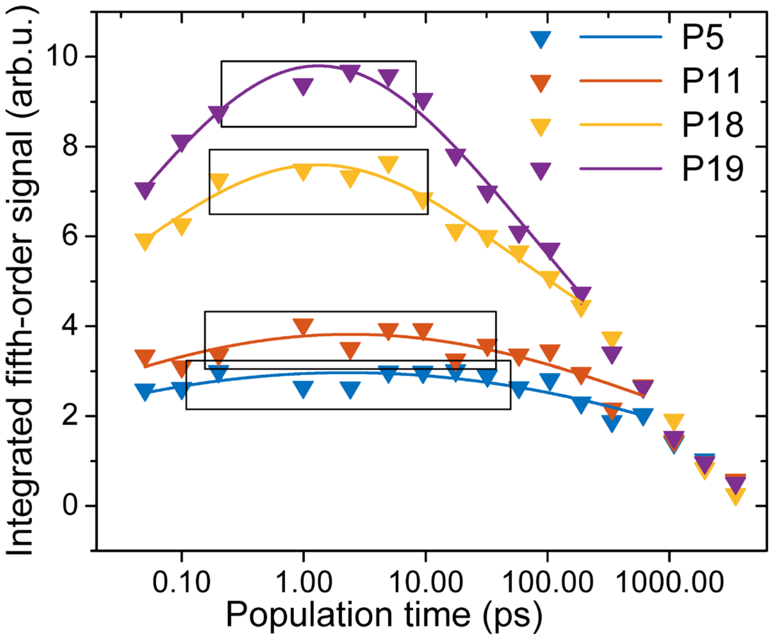

Figure S9. Extraction of EEI2D signal plateau regions. The colored lines are Lorentzian fits (in logarithmic time axis) of the signal (symbols) around the maximum regions. The black rectangles denote the regions within which the signal exceeds 90% of its maximum value.

Transition from anomalous to normal diffusion

Here we present an exemplary calculation that illustrates the transition from the trapped, anomalous diffusion of the excitons as discussed in the main paper to the conventionally assumed normal diffusion. Such a transition may occur if the excitons are small relative to the polymer size (in the illustrative calculation here adjusted by modifying the coupling between the chromophores J_{AB}), and if the excitons have the ability to escape energetic traps (in the illustrative calculation here adjusted by increasing the temperature T and assuming a broader spectrum of bath vibrational modes, i.e., a faster bath with large inverse correlation time Λ).

To demonstrate the transition from sub-diffusive to normal diffusive behavior without having to take into account any significant influence of the finite size, we calculate the exciton dynamics on a hypothetical P80 polymer that is much longer than the actual systems investigated experimentally. We set as an initial condition the population of the middle dimer. Again, in reality, the initial excitation may be located at various positions within the polymer chain, but for studying the transport property of a single exciton, we can choose to start in the center to have maximum propagation distance available until the end of the polymer is reached.

Shown in Fig. S10 is the time evolution of the mean square displacement, together with snapshots of the excitation probability distributions. In all cases the dynamics consist of three phases: an early "acceleration phase" indicative of the initial delocalization, (sub-)diffusive motion at intermediate times, and equilibration at later times when reaching the polymer ends. This is fully consistent with previous work[11,12] on delocalized exciton transport in disordered systems.

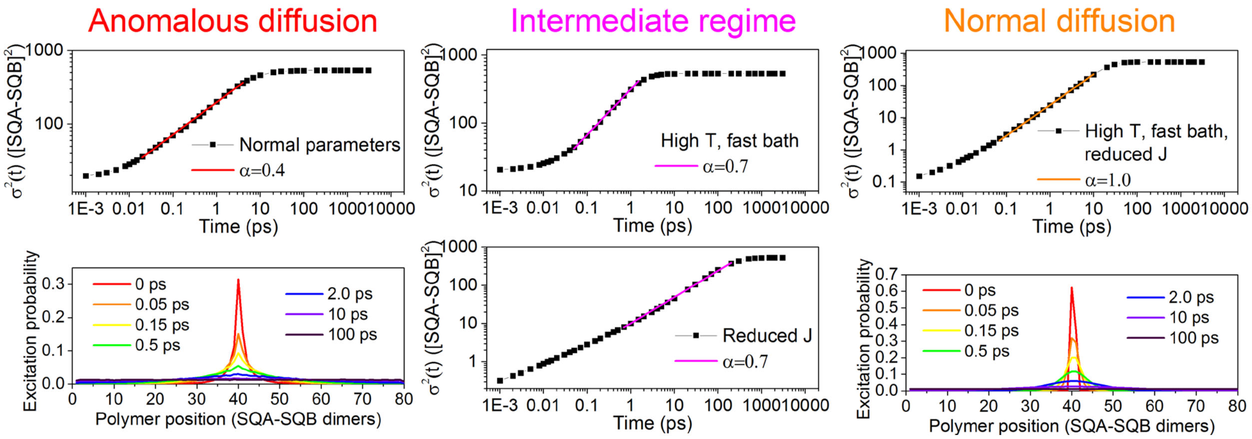

Figure S10. Transition from the anomalous diffusion to normal diffusion. Left: the anomalous diffusion regime in the measured squaraine copolymers, signified by the coefficient $\alpha = 0.4$ and the cusp shape of the excitation probability. Middle: intermediate regime, achieved either by high-temperature, fast bath limit (top), or by increased exciton localization and decreased exciton splitting by reducing the electronic inter-chromophoric coupling *J* (bottom). Right: normal diffusion regime, signified by the linear dependence of the mean-square displacement on time and the Gaussian shape of the excitation probability. The high-temperature limit was taken for the overdamped Brownian oscillator spectral density, and a "fast bath" realized by setting the bath correlation time down to 11 fs. The decrease of the coupling *J* from $420\ \mathrm{cm}^{-1}$ to $42\ \mathrm{cm}^{-1}$ was accompanied with an increase of the reorganization energy, to compensate for the slowdown of the Redfield rates in the weak coupling limit. This re-scaling only assures that the diffusive behavior develops on a reasonable timescale, and does not influence the diffusion character, see text for details.

We also present in Fig. S10 a power dependence $\sigma^2(t) = Dt^\alpha$, fitted to the steepest linear slope to determine the character of the (sub-)diffusive phase. We observe a transition from $\alpha = 0.4$ in the anomalous regime (as deduced for our experimental situation and discussed in the main manuscript) to $\alpha = 1$ signifying normal diffusion. The latter is reached for (in our actual polymer case, unphysically) high temperatures and a very short bath correlation time (practically flat spectrum of bath phonons). In the excitation probability distributions, we observe that the cusp shape, characteristic for trapped excitons, changes into a near-Gaussian shape as expected for normal diffusion.

To shift the timescale of the observed dynamics into the observed time window, we rescaled the bath reorganization energy for the ten times weaker coupling. Note that in the Redfield theory this merely rescales the population transfer rates. From the master equation for the density matrix (above on page 7), it is clear that this is equivalent to rescaling of the time axis. And this merely changes the diffusion coefficient D and not the power-law coefficient ($k \to \epsilon k \ \Rightarrow \ t \to \epsilon^{-1} t \ \Rightarrow Dt^\alpha \to (D\epsilon^{-\alpha})t^\alpha$). In our calculations we used $\epsilon = 1000$, which has no physical significance as the Redfield approximation is not quantitatively correct for localized excitons.

Inter-chain transfer discussion

In aggregated polymers or in solid state such as thin films, where the distance between the chains is small, exciton transfer between the polymer chains can take place.[13] In our experiments in diluted solution these effects are improbable for the following reasons. First, we can rule out polymer aggregation, based on the absence of concentration dependence of the measured linear spectra and fluorescence decay, in the concentration range used for the measurements. The possibility of inter-polymer transfer can be quantified by calculating the average distance between the polymers and comparing it to the Förster radius. The concentration was calculated by using the extinction coefficients from Table S2. Hereby, we assumed that the extinction coefficient of the polymer scales linearly with the chain length. Assuming point like particles, each polymer occupies a spherical volume of radius

$$R = \sqrt[3]{\frac{3}{4\,\pi\,N_A c}},$$

in which c is the concentration of the corresponding polymer and N_A the Avogadro number. The concentrations varied from 14 µmol/L for P5 to 3 µmol/L for P19. From this, the calculated average distance between the polymers (*2R*) is $\sim 80\ \mathrm{nm}$ (varying from 60 nm for P5 to 100 nm for P19). To estimate if inter-chain transfer has to be taken into account, we calculated the Förster radius R_0 using the formula[14]

$$R_0 = \left(\frac{\kappa^2 \Phi_D J^\lambda}{n^4}\right)^{\frac{1}{6}}.$$

Here κ^2 is the orientation factor, Φ_D the fluorescence quantum yield, J^λ the spectral overlap integral and n the refractive index of the solvent. The orientation factor was fixed to $\kappa^2 = 2/3$ as isotropic. The spectral overlap integral was calculated from the corresponding absorption and emission spectra. The Förster radius was found to be $\sim 10\ \mathrm{nm}$ (increasing from 7 nm for P5 to 11.5 nm for P19). Relating this to the average distance of $\sim 80\ \mathrm{nm}$, the inter-polymer transfer is thus very unlikely to happen. Ruling out the inter-chain transfer within the same polymer is harder, as we have no indication of the polymer morphology. In our description we assume that the intrachain coupling is much stronger than the interaction between the chains. This can be partially justified by the relatively short polymers and the additional stabilizing effect of the toluene as a solvent.

S2 Characterization

General information

Synthetic work was carried out in standard glassware. Chemicals purchased were used without further purification. Nitrogen used for reactions under inert gas atmosphere was dried over Sicapent® by Merck and oxygen was removed by copper oxide catalyst R3-11 by BASF. Solvents were dried according to standard literature procedure and stored under nitrogen atmosphere. Reactions under inert gas atmosphere were performed in flame-dried schlenk flask using standard schlenk methods. Flash column chromatography was performed on silica gel (40 – 63 µm, Macherey-Nagel "Silica 60 M") in glass columns.

Steady-state emission spectroscopy

Steady-state emission spectra were measured on a FLS980 fluorescence lifetime spectrometer (software F980 version 1.2.2, 450 W Xenon lamp, PMT Hamamatsu R5509-42) by Edinburgh Instruments. Emission spectra were recorded at 298 K in 1 cm quartz cuvettes by Starna (Pfungstadt, Germany) using highly diluted samples (λ_{max} < 0.05 OD) to prevent self-absorption. Quantum yields (see Table S2) were determined with optically dense samples in an integrating sphere and corrected afterwards for self-absorptions using the method of Bardeen et al.[15] The quartz cuvette as well as the volumetric flasks were silylated in order to prevent unwanted adsorption or other interactions with the glass surface.[16]

Time-dependent emission spectroscopy

Time-correlated single-photon counting (TCSPC) was performed on a FLS980 fluorescence lifetime spectrometer (software F980 version 1.2.2) with a 656 nm pulsed laser diode at low power (10 pJ/pulse) and a high speed PMT (Hamamatsu H10720-01) under magic angle conditions. Sample preparation was similar to the steady-state emission experiments. A fit with multiple exponential functions of the decay curves was processed by the FAST software (version 3.4.2) via deconvolution of the data (4096 channels) and the instrument response function (IRF). The fits together with the residuals are displayed in Fig. S9 for completeness. As for the IRF measurement a solution consisting of colloidal silica in deionised water (LUDOX) was used. The fitted values are in Table S2.

NMR spectroscopy

^{1}H-NMR spectra were measured using either Avance III HD 400 FT-Spectrometer (^{1}H: 400.13 MHz, with a Bruker Ultrashield magnet) or Avance III HD 400 FT-Spectrometer (^{1}H: 400.03 MHz, with a Bruker Ascend magnet). High sample concentrations of > 0.1 mM in deuterated solvents ($CDCl_3$) were used. The chemical shifts are displayed in ppm relative to nondeuterated solvent signal (^{1}H: $CHCl_3$: δ7.26 ppm). The abbreviations used for the spin multiplicities are: s = singlet, d = doublet, t = triplet, q = quartet, m = multiplet, dd = doublet of doublet, ddd = doublet of doublet of doublet. Multiplet signals or overlapping multiplet signals that could not be assigned to first order coupling are given as (-). The coupling constants are given in Hertz (Hz). Order of description for ^{1}H NMR spectra: chemical shift (spin multiplicity, coupling constant, number of protons, assignment).

Mass spectrometry

High resolution mass spectra (ESI) were measured with a Bruker Daltonics microTOF focus. Peaks are reported as m/z. For calculation of the respective mass values of the isotopic distribution, the software Compass 1.1 (Bruker Daltonics GmbH, Bremen) was used. Calculated (calc.) and measured (found) peak values always correspond to the most intense peak of the isotopic distribution.

Gel Permeation Chromatography (GPC)

For preparative procedures the Shimadzu recycling GPC-system (diode array detector: SPD-M20A, CBM-20A (system controller), LC-20AD (solvent delivery unit), DGU-20A9 (online degasser), solvent: $CHCl_3$, temperature: 20 °C) was used with two SDV columns (100 Å, 1000 Å, particle size 10 µm, 20 × 600 mm; PSS, Mainz, Germany).

For analytical measurements the same system was used with an analytical SDV column "Linear S" (mixed bed, particle size 5 µm, 8 × 300 mm; PSS, Mainz, Germany). Polystyrene (1 mg/mL) was used as calibration standard.

Linear spectroscopy data

Table S2 summarizes the spectroscopic data of each fraction.

Table S2. Absorption maxima $\tilde{\nu}_{max}$ and λ_{max}, extinction coefficients ε_{max}, fluorescence maxima $\tilde{\nu}_{fl}$ / cm^{-1} and λ_{fl}, fluorescence quantum yields Φ_{fl}, and fluorescence lifetimes τ of each polymer fraction in toluene. The bi-exponential fit errors χ^2 are also given for completeness. Extinction coefficients are displayed per monomer unit (i.e., per SQA–SQB dimer).

	$\tilde{\nu}_{max}$ / cm^{-1} (λ_{max} / nm)	ε_{max} / L mol^{-1} cm^{-1}	$\tilde{\nu}_{fl}$ / cm^{-1} (λ_{fl} / nm)	Φ_{fl} / %	τ / ns[a]	χ^2
P19	12700 (790)	$3.71 \cdot 10^5$	12600 (791)	24	0.49 (0.51) 1.56 (0.49)	1.677
P18	12700 (789)	$2.99 \cdot 10^5$	12600 (791)	38	0.68 (0.53) 1.87 (0.47)	1.463
P11	12700 (787)	$2.18 \cdot 10^5$	12600 (791)	40	0.95 (0.57) 2.18 (0.43)	1.289
P5	13200 (755)	$1.83 \cdot 10^5$	12700 (789)	29	1.44 (0.76) 4.01 (0.24)	1.179

[a](Multi-)exponential fit of fluorescence decay measured by TCSPC, excitation was at 15200 cm^{-1} (656 nm). Amplitudes are given in brackets. Fluorescence was detected at their respective maxima.

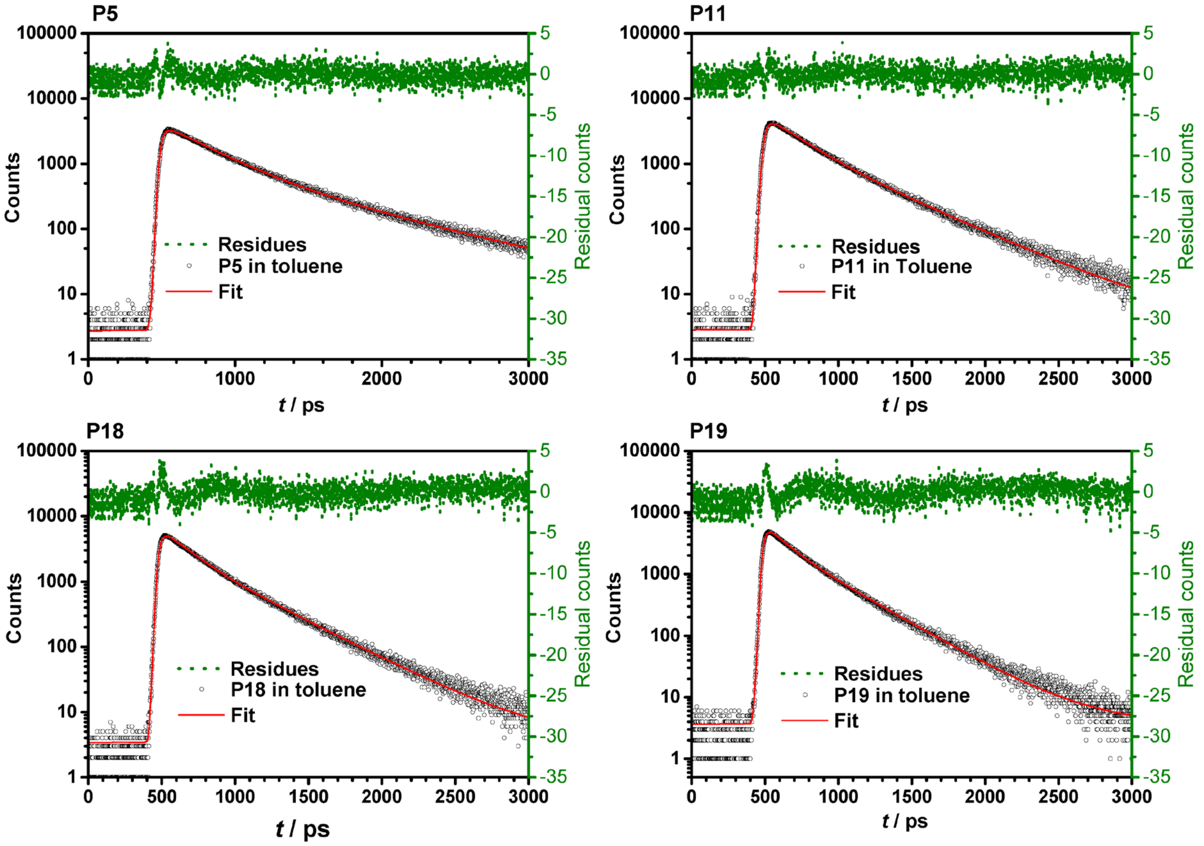

Figure S11. TCSPC decay curves for the four polymer lengths, together with the fitted two-exponential decays (red) and the residuals (green). The determined lifetimes and amplitudes are in Table S2.

Laser spectra

In Fig. S12 we show, for completeness, the employed pump and broadband probe spectra, demonstrating that we probe the whole spectral region of the one-exciton states in the studied SQA-SQB copolymers. The probe pulse fully covers the low-energy red states of relaxed excitons, probing the on-average-isoenergetic dynamics of locally relaxed excitons along the polymer chain. Structured probe spectra, such as the one here, are commonly used in transient absorption measurements. The shape itself is not particularly relevant due to the differential acquisition of the signal. Any possible accompanying dispersion of the probe pulse makes the time-zero spectra less reliable. However, as we do not discuss lineshapes and focus instead on the signal kinetics, the time-zero uncertainty is not of crucial importance. The pump pulses are compressed with the assistance of our DAZZLER (Fastlite) shaper to about 14 fs, characterized by collinear FROG measurement.

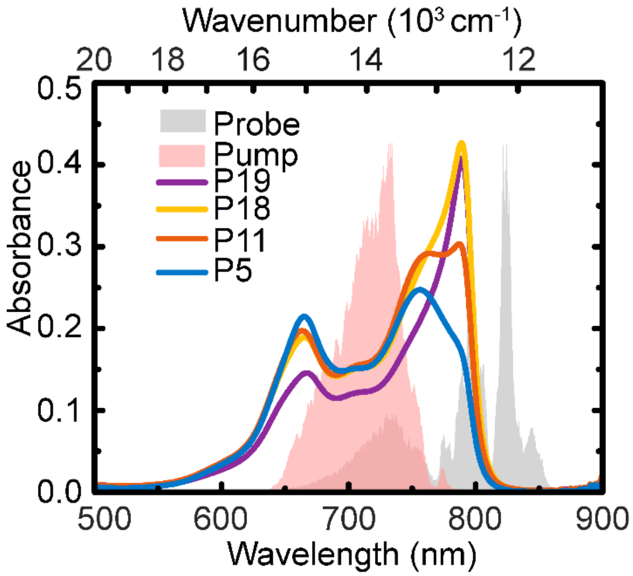

Figure S12. Laser pump (gray shaded area) and probe spectra (orange shaded area) used for the EEI2D measurement in comparison to the linear absorption spectra of the four polymer samples.

S3 Synthesis

Synthesis of SQA-Br_2

The precursors 5-bromo-2,3,3-trimethyl-3*H*-indole,[17] 1-iodo-3,7-dimethyloctane[18] and the resulting quaternary salt[19,20] were synthesized according to given literature procedures.

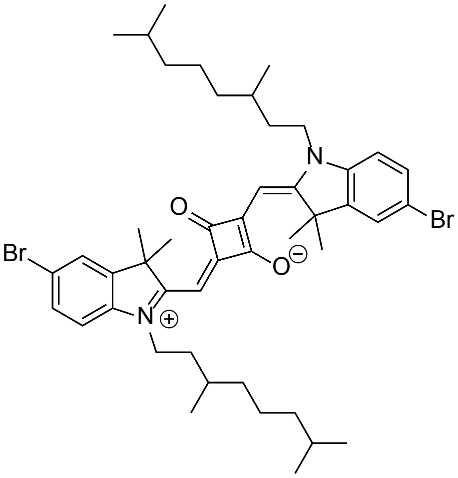

Synthesis according to literature.[21]

5-Bromo-1-(3,7-dimethyloctyl)-2,3,3-trimethyl-3*H*-indol-1-ium iodide (4.00 g, 7.90 mmol, 2.5 eq.) and 3,4-dihydroxycyclobut-3-ene-1,2-dione (360 mg, 3.16 mmol, 1.0 eq) were dissolved in a 1:1 mixture of *n*-butanol/toluene (60 mL). Pyridine (10 mL) was added and the mixture was refluxed for 17 h using a *Dean-Stark* apparatus. The solvent was evaporated under reduced pressure and the residue was purified by flash column chromatography (DCM/MeOH 99.5:0.5 → 98.5:1.5). The crude product was dissolved in a small amount of DCM and dropped into an excess of *n*-hexane. The resulting crystals were filtered off and dried under high vacuum.

<u>Yield</u>: 2.34 g, (2.80 mmol, 89 %) of a green solid.

$C_{46}H_{62}Br_2N_2O_2$ [834.82]

^{1}**H-NMR** (400 MHz, $CDCl_3$, 300 K):

δ [ppm] = 7.44 (d, $^4J_{HH}$ = 1.8 Hz, 2H, 2x -C$\underline{H}$-), 7.42 (dd, $^3J_{HH}$ = 8.3 Hz, $^4J_{HH}$ = 1.9 Hz, 2H, 2x -C$\underline{H}$-), 6.82 (d, $^3J_{HH}$ = 8.3 Hz, 2H, 2x -C$\underline{H}$-), 5.95 (s, 2H, 2x -CC$\underline{H}$C-), 4.06 – 3.85 (m, 4H, 2x -NC$\underline{H_2}$-), 1.85 – 1.45 (-, 8H, 2x –$NCH_2C\underline{H_2}$-, 2x -C$\underline{H}$$CH_3$, 2x -C$\underline{H}$$(CH_3)_2$), 1.77 (s, 12H, 2x -C(C$\underline{H_3})_2$), 1.40 – 1.10 (-, 12H, 2x -C$\underline{H_2}$C$\underline{H_2}$C$\underline{H_2}$-), 1.03 (d, $^3J_{HH}$ = 6.2 Hz, 6H, 2x -CHC$\underline{H_3}$), 0.86 (d, $^3J_{HH}$ = 6.6 Hz, 12H, 2x -CH(C$\underline{H_3})_2$).

ESI-MS (pos., high res.): [$MNa^{\bullet +}$]

calc.: 857.3055 m/z

found: 857.3056 m/z Δ = 0.08 ppm

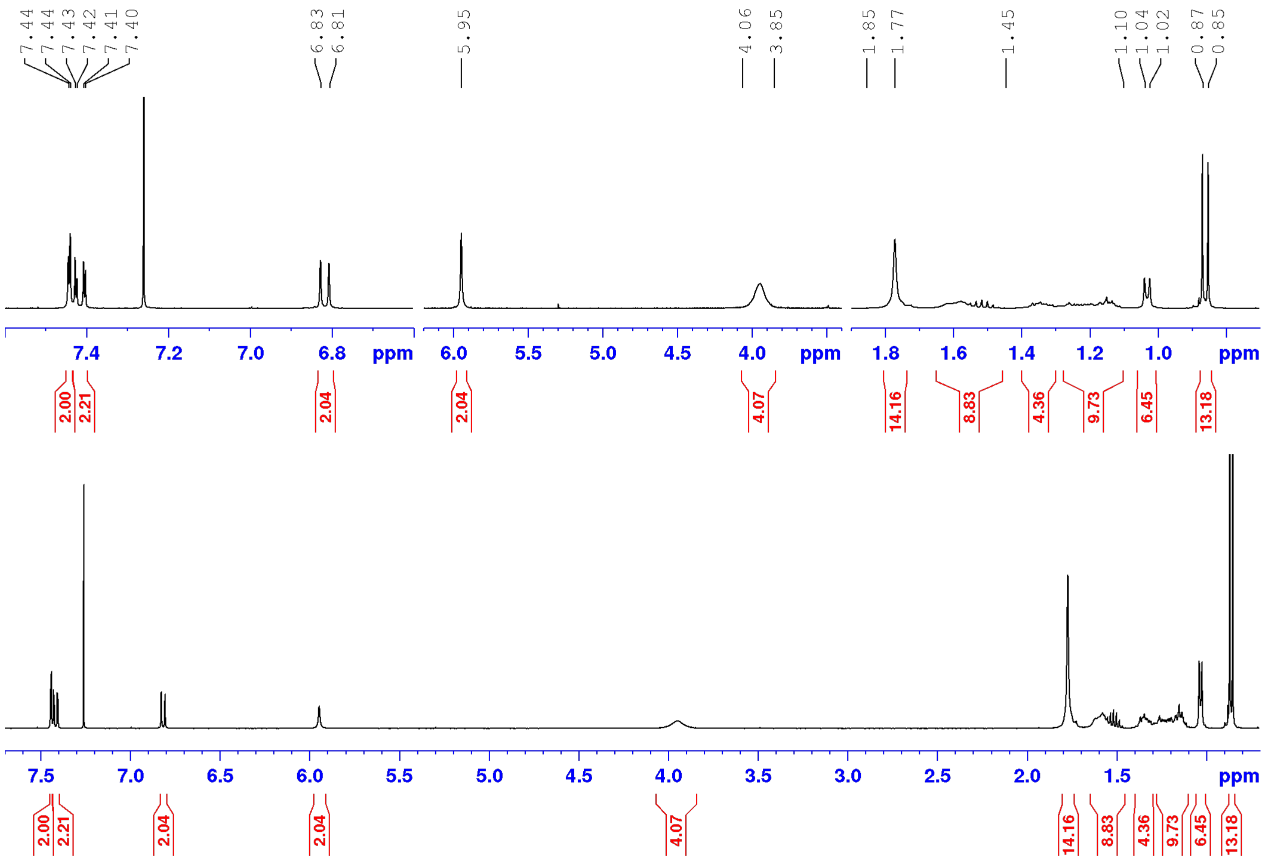

Figure S13. ^{1}H NMR ($CDCl_3$, 400 MHz) spectrum of SQA-Br_2.

Synthesis of SQA-(Bpin)$_2$

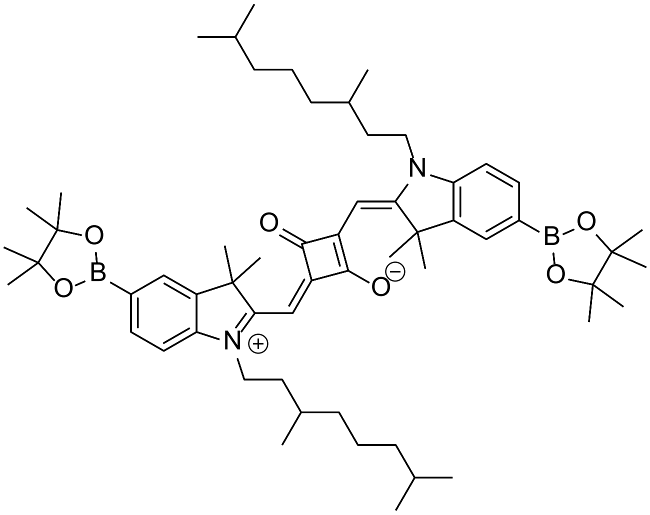

Synthesis according to literature.[21]

Under nitrogen atmosphere SQA-Br$_2$ (2.34 g, 2.80 mmol, 1.0 eq), bis(pinacolato)diboron (1.99 g, 7.85 mmol, 2.8 eq) and KOAc (880 mg, 8.97 mmol, 3.2 eq) were dissolved in dry 1,4-dioxane (40 mL). The solution was purged with a gentle stream of nitrogen for 15 min. Pd(dppf)Cl$_2$ · CH$_2$Cl$_2$ (114 mg, 140 µmol, 0.05 eq) was added and the reaction was continuously heated at 115 °C for 18 h under exclusion of light. The solvent was filtrated and then evaporated under reduced pressure. The residue was purified by flash column chromatography (PE/EA 1:1 → DCM/EA 1:1), the crude product was dissolved in a small amount of DCM and dropped into an excess of *n*-hexane. The precipitate was filtered off and dried under high vacuum.

Yield: 1.74 mg, (1.87 mmol, 67 %) of a green solid.

$C_{58}H_{86}B_2N_4O_6$ [928.95]

^{1}**H-NMR** (400 MHz, CDCl$_3$, 300 K):

δ [ppm] = 7.78 (dd, $^{3}J_{HH}$ = 7.9 Hz, $^{4}J_{HH}$ = 1.1 Hz, 2H, 2 × -C$\underline{H}$-) 7.76 (-, 2H, 2 × -C$\underline{H}$-), 6.95 (d, $^{3}J_{HH}$ = 8.0 Hz, 2H, 2 × -C$\underline{H}$-), 5.99 (s, 2H, 2 × -CC$\underline{H}$C-), 4.10 – 3.90 (m, 4H, 2 × -NC$\underline{H_2}$-), 1.88 – 1.73 (m, 2H, 2 × -NCH$_2$C$\underline{H_2}$-), 1.79 (s, 12H, 2 × -C(C$\underline{H_3}$)$_{\underline{2}}$), 1.62 – 1.45 (-, 6H, 2 × -NCH$_2$C$\underline{H_2}$-, 2 × -C$\underline{H}$CH$_3$, 2 × -C$\underline{H}$(CH$_3$)$_2$), 1.40 – 1.10 (-, 12H, 2 × -C$\underline{H_2}$C$\underline{H_2}$C$\underline{H_2}$-), 1.36 (s, 24H, 4 × -OC(C$\underline{H_3}$)$_{\underline{2}}$), 1.03 (d, $^{3}J_{HH}$ = 6.2 Hz, 6H, 2 × -CHC$\underline{H_3}$), 0.86 (d, $^{3}J_{HH}$ = 6.6 Hz, 12H, 2 × -CH(C$\underline{H_3}$)$_{\underline{2}}$).

ESI-MS (pos., high res.): [M$^{\bullet +}$]

calc.: 928.6685 m/z

found: 928.6685 m/z Δ = 0.00 ppm

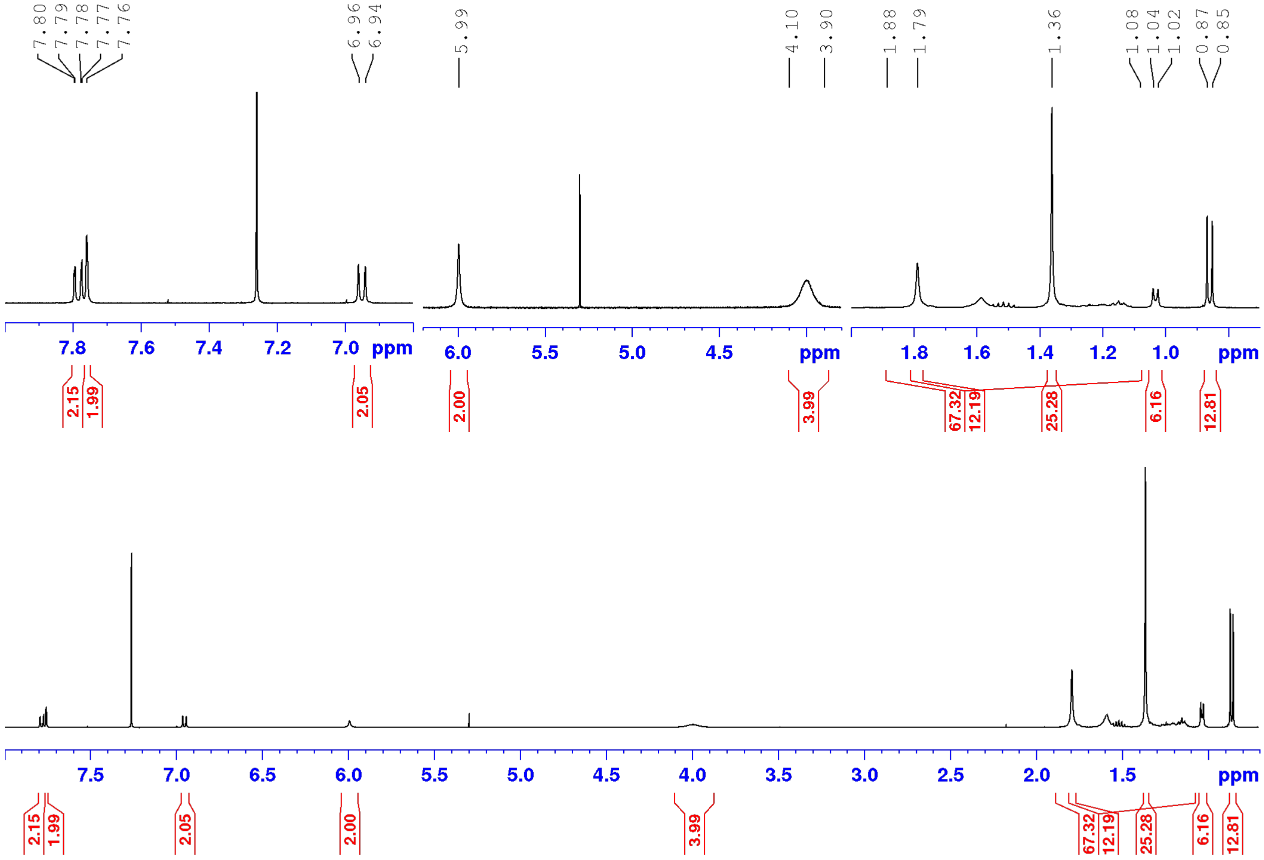

Figure S14. ^{1}H NMR (CDCl$_3$, 400 MHz) spectrum of SQA-B$_2$.

Synthesis of SQB-Br$_2$

The precursors 5-bromo-2,3,3-trimethyl-3*H*-indole,[17] 1-iodo-3,7-dimethyloctane,[18] the resulting quaternary salt[19,20] and triethylammonium 3-(dicyanomethylene)-2-ethoxy-4-oxocyclobut-1-en-1-olate[22] were synthesized according to given literature procedures.

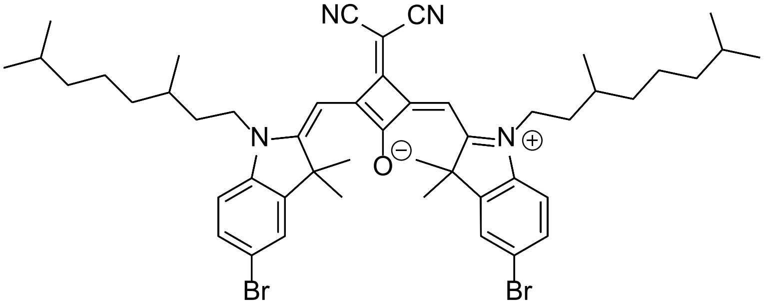

Synthesis according to literature.[21]

5-Bromo-1-(3,7-dimethyloctyl)-2,3,3-trimethyl-3*H*-indol-1-ium iodide (2.17 g, 4.94 mmol, 2.5 eq.) and triethylammonium 3-(dicyanomethylene)-2-ethoxy-4-oxocyclobut-1-en-1-olate (500 mg, 1.72 mmol, 1.0 eq) were dissolved in a 1:1 mixture of *n*-butanol/toluene (60 mL). Pyridine (10 mL) was added and the mixture was refluxed for 17 h using a *Dean-Stark* apparatus. The solvent was evaporated under reduced pressure and the residue was purified by flash column chromatography (DCM). The crude product was dissolved in a small amount of DCM and dropped into an excess of *n*-hexane. The precipitate were filtered off and dried under high vacuum.

Yield: 1.20 g, (1.36 mmol, 79 %) of a purple solid.

$C_{49}H_{62}Br_2N_4O$ [882.87]

^{1}H-NMR (400 MHz, $CDCl_3$, 300 K):

δ [ppm] = 7.48 – 7.44 (-, 4H, 4 × -C$\underline{H}$-), 6.89 (d, $^{3}J_{HH}$ = 8.1 Hz, 2H, 2 × -C$\underline{H}$-), 6.49 (s, 2H, 2 × -CC$\underline{H}$C-), 4.10 – 3.90 (m, 4H, 2 × -NC$\underline{H_2}$-), 1.81 – 1.70 (m, 2H, 2 × -$NCH_2C\underline{H_2}$-), 1.76 (s, 12H, 2 × -C(C$\underline{H_3}$)$\underline{_2}$), 1.68 – 1.45 (-, 6H, 2 × -$NCH_2C\underline{H_2}$-, 2 × -C$\underline{H}$$CH_3$, 2 × -C$\underline{H}$$(CH_3)_2$), 1.41 – 1.10 (-, 12H, 2 × -C$\underline{H_2}$C$\underline{H_2}$C$\underline{H_2}$-), 1.01 (d, $^{3}J_{HH}$ = 6.4 Hz, 6H, 2 × -CHC$\underline{H_3}$), 0.86 (d, $^{3}J_{HH}$ = 6.6 Hz, 12H, 2 × -CH(C$\underline{H_3}$)$\underline{_2}$).

ESI-MS (pos., high res.):

calc.: 905.3168 m/z

found: 905.3192 m/z Δ = 2.65 ppm

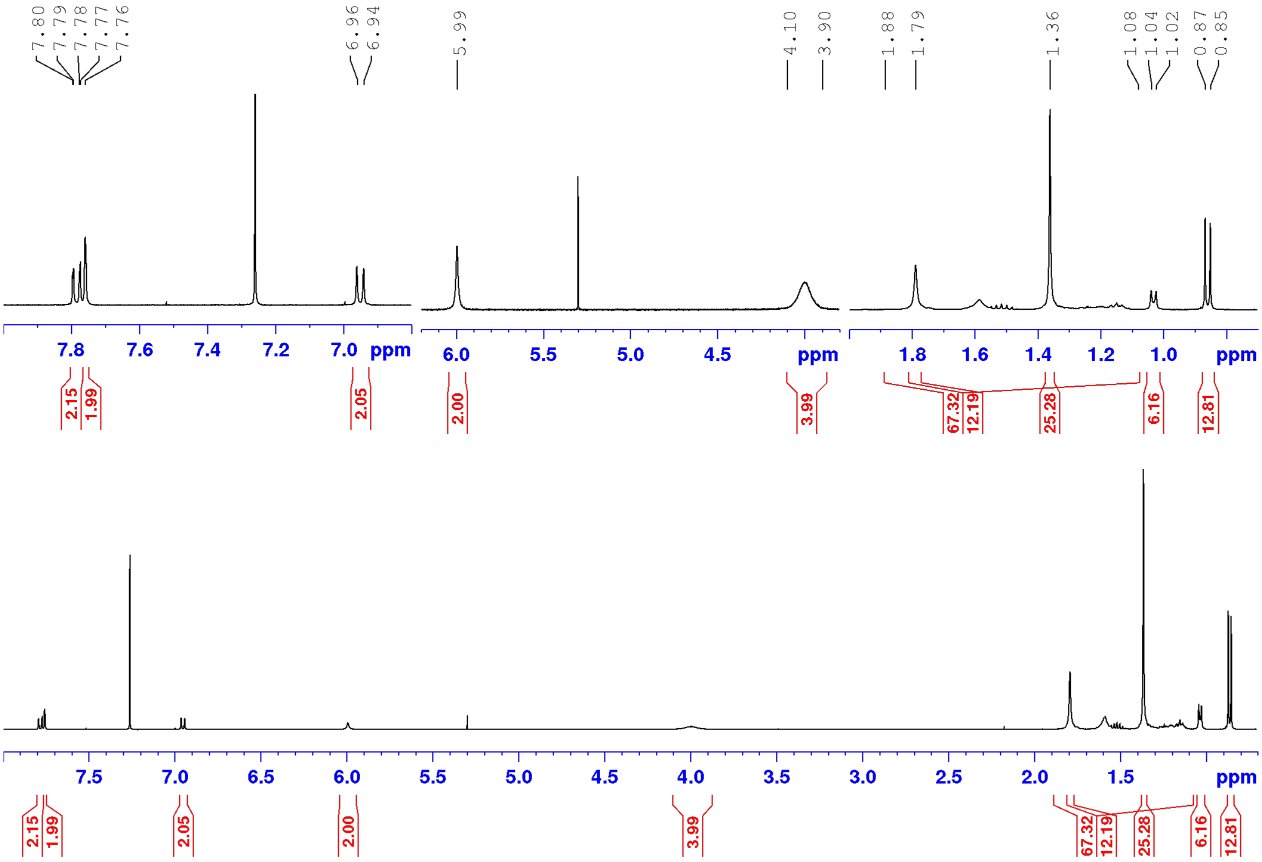

Figure S15. ^{1}H NMR ($CDCl_3$, 400 MHz) spectrum of SQB-Br_2.

Copolymerization of SQA-(Bpin)$_2$ and SQB-Br$_2$

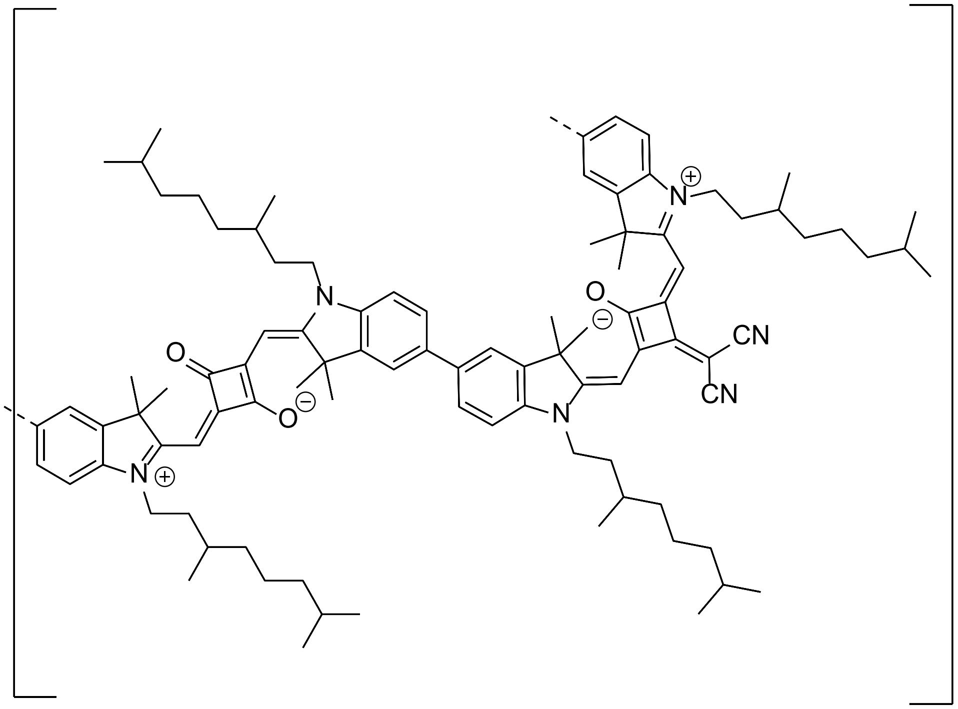

Synthesis according to literature.[5]

Under nitrogen atmosphere SQA-(Bpin)$_2$ (170 mg, 183 µmol, 1.0 eq), SQB-Br$_2$ (162 mg, 183 µmol, 1.0 eq) and NaHCO3 (615 mg, 7.32 mmol, 40 eq) were dissolved in a 4:1 mixture of THF/water (20 mL). The mixture was purged with a gentle stream of nitrogen for 15 min. Tetrakis(triphenylphosphine)palladium (4.23 mg, 3.66 µmol, 0.02 eq) was added and the reaction was continuously heated at 100 °C for 3 h under exclusion of light. The reaction was quenched with brine (20 mL) and CHCl$_3$ (20 mL) and the layers were separated. The organic layer was washed with brine (3 × 50 mL) and H$_2$O (50 mL) and dried over Na$_2$SO$_4$. After filtration the solvent was evaporated under reduced pressure. The crude product was further purified and fractionated by preparative GPC.

<u>Yield (crude)</u>: 270 mg (~189 µmol,~100 %) of ruby solid.

$(C_{95}H_{124}N_6O_3)_n$ $[1398.04]_n$

^{1}H-NMR (400 MHz, $CDCl_3$, 300 K):

δ [ppm] = 7.60 – 7.49 (-, 8H, 8 × $-C\underline{H}-$), 7.11 (d, $^3J_{HH}$ = 7.8 Hz, 2H, 2 × $-C\underline{H}-$), 7.06 (d, $^3J_{HH}$ = 8.3 Hz, 2H, 2 × $-C\underline{H}-$), 6.54 (s, 2H, 2 × $-CC\underline{H}C-$), 6.05 (s, 2H, 2 × $-CC\underline{H}C-$), 4.25 – 3.90 (-, 8H, 2 × $-NC\underline{H_2}-$), 2.05 – 1.11 (-, 40H, 4 × $-NCH_2C\underline{H_2}-$, 4 × $-C\underline{H}CH_3$, 4 × $-C\underline{H}(CH_3)_2$, 4 × $-C\underline{H_2}C\underline{H_2}C\underline{H_2}-$), 1.86 (s, 12H, 2 × $C(C\underline{H_3})_2$), 1.84 (s, 12H, 2 × $C(C\underline{H_3})_2$), 1.07 (d, $^3J_{HH}$ = 6.0 Hz, 6H, 2 × $-CHC\underline{H_3}$), 1.05 (d, $^3J_{HH}$ = 6.2 Hz, 6H, 2 × $-CHC\underline{H_3}$), 0.873 (d, $^3J_{HH}$ = 6.6 Hz, 12H, 2 × $-CH(C\underline{H_3})_2$), 0.868 (d $^3J_{HH}$ = 6.6 Hz, 12H, 2 × $-CH(C\underline{H_3})_2$).

Due to the polymeric nature the NMR signals are broadened in comparison to the monomers.

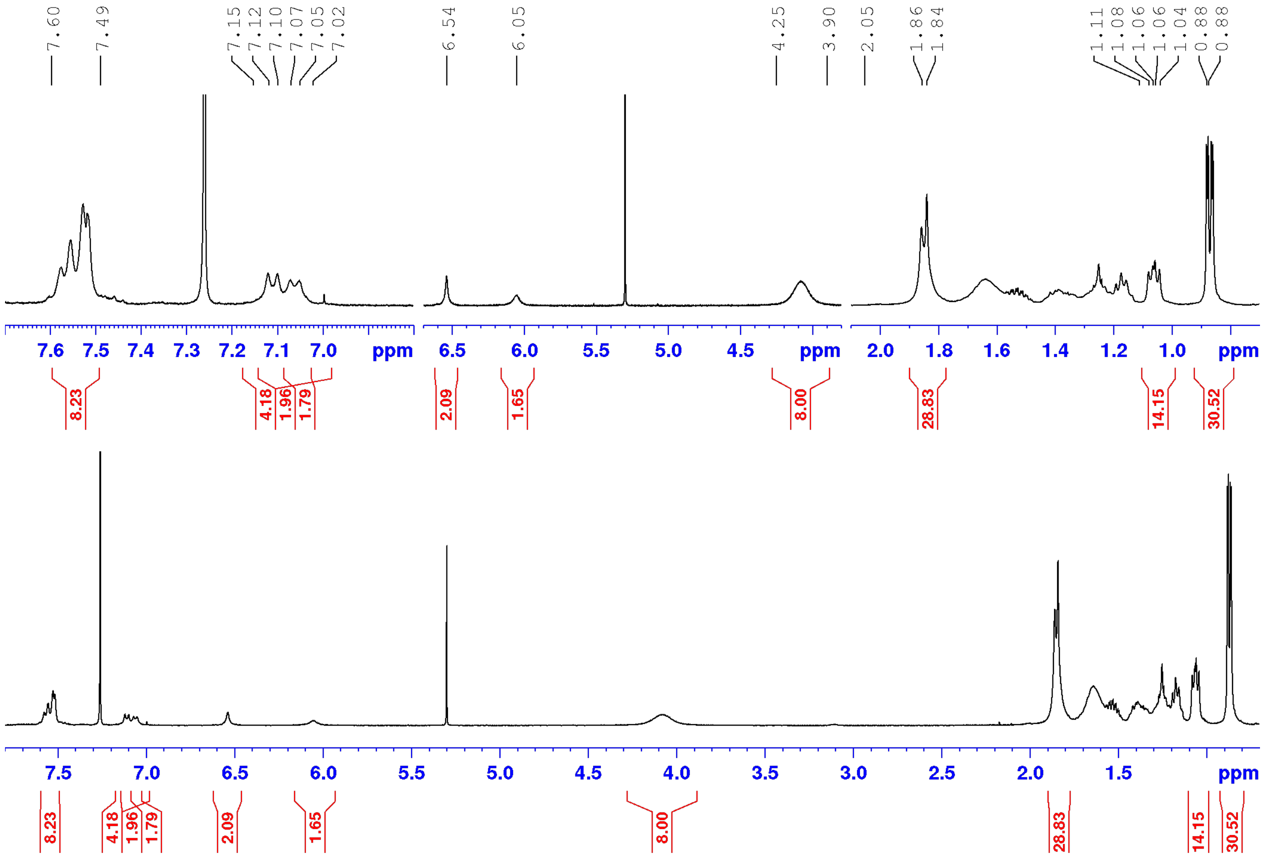

Figure S16. ^{1}H NMR ($CDCl_3$, 400 MHz) spectrum of $[SQA\text{-}SQB]_N$ copolymer.

Polymerization Data

By use of the preparative GPC ($CHCl_3$) the crude copolymer was partitioned into five sections by splitting the polymer at specific times (see Table S3). A sample of the original polymer, as well as each fraction were then analyzed via the analytical GPC ($CHCl_3$), using the polystyrene calibration as a default comparison. The measured data are reported below. Figures S17 and S18 show the recorded GPC data plotted against time and repeating unit, respectively.

Table S3. GPC data of each fraction. M_n is the number average molecular mass, M_w the mass average molecular mass, M_z the centrifugation average molecular mass, $Đ$ the polydispersity of the polymer and X_n the degree of polymerization with $[SQA–SQB]_1$ as the repeating unit.

	Cut / min	M_n / g mol^{-1}	M_w / g mol^{-1}	M_z / g mol^{-1}	$Đ$	X_n
Crude Mix	–	13000	33800	68300	2.60	9
P19	39.75 – 41.00	26200	42400	65800	1.62	19
P18	– 42.50	24700	38000	56500	1.54	18
P11	– 44.00	15200	32200	51600	2.11	11
P5	– 46.50	7300	20900	44700	2.88	5

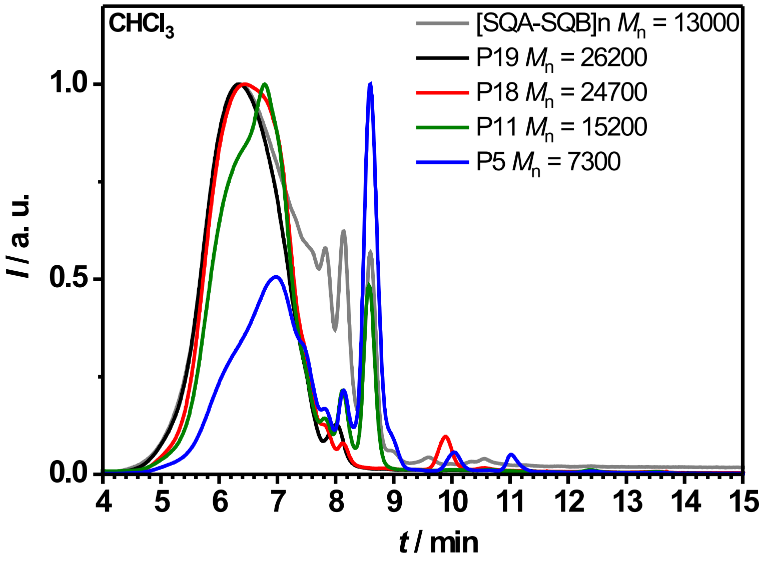

Figure S17. Normalized GPC data plotted against time.

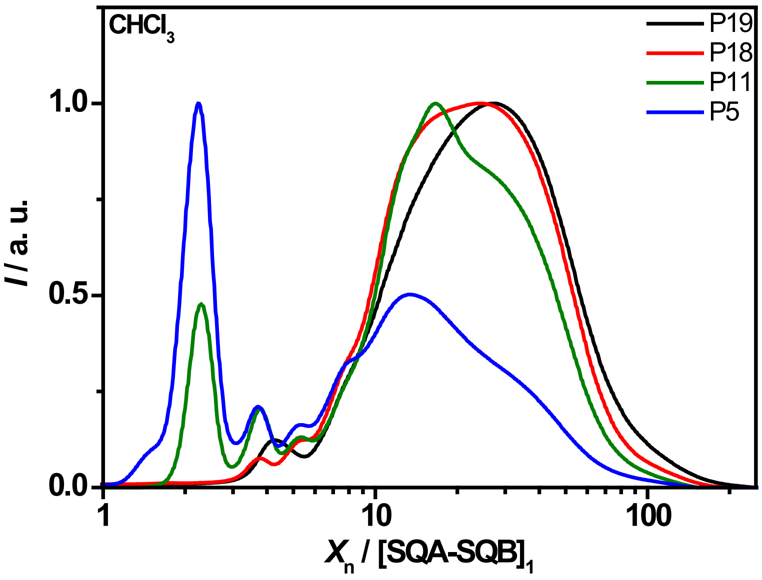

Figure S18. Normalized GPC data (vs. PS) plotted against degree of polymerization.

As shown in Fig. S15 smaller polymer fractions like P5 are composed of a higher proportion of small oligomers and, in P5's case, potential cyclomers, while P18 and above extend into a regime of over 150 repeating units.

Using the *Carothers* equation an estimated turnover number can be calculated:

$$X_n = \frac{1}{1-p}.$$

X_n is the degree of polymerization, p the extent of reaction/conversion to polymer. For $X_n = 9$, p equals to 0.89. A conversion of 89 % is also reflected in the near quantitative yield of the *Suzuki* coupling, in which only little monomer could be found.

In two works of Höger et al. it is stated that the polystyrene calibrated GPC (THF) overestimates the molecular weight of their oligo(*p*-phenylene-butadiynylene) compounds (up to 60 repeating units).[23,24] Since the oligomers behave like a rod and are therefore not malleable, unlike polystyrene, a general predication cannot be made for other polymers. As for the squaraine copolymers, a mixture of elongated zig-zag, helical and other superstructures is expected to exist in $CHCl_3$, due to the SQB building block.[5,19] The ^1H NMR spectra show only broadened signals due to the polydisperse nature of the compound; no features of a proton from either end of the polymer are apparent (see Fig. S16).

References

1 Volkhard May and Oliver Kühn, *Charge and Energy Transfer Dynamics in Molecular Systems*, Wiley-VCH Verlag GmbH, 2nd edition., 2004.
2 V. I. Novoderezhkin, M. A. Palacios, H. van Amerongen and R. van Grondelle, *J. Phys. Chem. B*, 2004, **108**, 10363–10375.
3 Leonas Valkunas, Darius Abramavicius, Tomáš Mančal, *Molecular Excitation Dynamics and Relaxation*, WILEY-VCH, Weinheim, 1st edn., 2013.
4 M. I. S. Röhr, H. Marciniak, J. Hoche, M. H. Schreck, H. Ceymann, R. Mitric and C. Lambert, *J. Phys. Chem. C*, 2018, **122**, 8082–8093.
5 S. F. Völker, A. Schmiedel, M. Holzapfel, K. Renziehausen, V. Engel and C. Lambert, *J. Phys. Chem. C*, 2014, **118**, 17467–17482.
6 K. Hader, V. May, C. Lambert and V. Engel, *Phys. Chem. Chem. Phys.*, 2016, **18**, 13368–13374.
7 H. Yamagata and F. C. Spano, *J. Phys. Chem. Lett.*, 2014, **5**, 622–632.
8 F. C. Spano and C. Silva, *Annu. Rev. Phys. Chem.*, 2014, **65**, 477–500.
9 K. H. Park, W. Kim, J. Yang and D. Kim, *Chem. Soc. Rev.*, 2018, **47**, 4279–4294.
10 C. Heshmatpour, J. Hauer and F. Šanda, *Chemical Physics*, 2019, 110433.
11 W. Barford and C. D. P. Duffy, *Phys. Rev. B*, 2006, **74**, 075207.
12 R. Dutta and B. Bagchi, *The Journal of Chemical Physics*, 2016, **145**, 164907.
13 B. J. Schwartz, *Annu. Rev. Phys. Chem.*, 2003, **54**, 141–172.
14 S. E. Braslavsky, E. Fron, H. B. Rodríguez, E. S. Román, G. D. Scholes, G. Schweitzer, B. Valeur and J. Wirz, *Photochem. Photobiol. Sci.*, 2008, **7**, 1444–1448.
15 T.-S. Ahn, R. O. Al-Kaysi, A. M. Müller, K. M. Wentz and C. J. Bardeen, *Rev. Sci. Instrum.*, 2007, **78**, 086105.
16 G. A. Olah, S. C. Narang, B. G. B. Gupta and R. Malhotra, *J. Org. Chem.*, 1979, **44**, 1247–1251.
17 M. V. Reddington, *Bioconjugate Chem.*, 2007, **18**, 2178–2190.
18 C. J. Bennett, S. T. Caldwell, D. B. McPhail, P. C. Morrice, G. G. Duthie and R. C. Hartley, *Bioorg. Med. Chem.*, 2004, **12**, 2079–2098.
19 S. F. Völker and C. Lambert, *Chem. Mater.*, 2012, **24**, 2541–2553.
20 S. F. Völker, S. Uemura, M. Limpinsel, M. Mingebach, C. Deibel, V. Dyakonov and C. Lambert, *Macromol. Chem. Phys.*, 2010, **211**, 1098–1108.
21 S. F. Völker, T. Dellermann, H. Ceymann, M. Holzapfel and C. Lambert, *J. Polym. Sci. Part A: Polym. Chem.*, 2014, **52**, 890–911.
22 R. I. Zubatyuk, V. N. Baumer, A. L. Tatarets, L. D. Patsenker and O. V. Shishkin, *Acta Crystallogr., Sect. E: Struct. Rep. Online*, 2004, **60**, o2252–o2254.
23 F. Hinderer, R. May, S.-S. Jester and S. Höger, *Macromolecules*, 2016, **49**, 1816–1821.
24 D. Mössinger, S.-S. Jester, E. Sigmund, U. Müller and S. Höger, *Macromolecules*, 2009, **42**, 7974–7978.